Controlled Fabrication of Native Ultra-Thin Amorphous Gallium Oxide from 2D Gallium Sulfide for Emerging Electronic Applications

AbdulAziz AlMutairi[1,2], Aferdita Xhameni[2,3], Xuyun Guo[4,5,6], Irina Chircă[1], Valeria Nicolosi[4,5,6], Stephan Hofmann[1], Antonio Lombardo[2,3]

[1]Department of Engineering, University of Cambridge, United Kingdom

[2]London Centre for Nanotechnology, 19 Gordon St, London, WC1H 0AH, United Kingdom

[3]Department of Electronic & Electrical Engineering, Malet Place, University College London, WC1E 7JE, United Kingdom

[4]Advanced Materials and BioEngineering Research (AMBER), Centre at Trinity College Dublin and the Royal College of Surgeons in Ireland, Dublin, 2, Ireland

[5]Trinity Centre for Biomedical Engineering, Trinity College Dublin, Dublin, 2, Ireland

[6]School of Chemistry, Trinity College Dublin, Dublin, 2, Ireland

Abstract

Oxidation of two-dimensional (2D) layered materials has proven advantageous in creating oxide/2D material heterostructures, opening the door for a new paradigm of low-power electronic devices. Gallium (II) sulfide (β-GaS), a hexagonal phase group III monochalcogenide, is a wide bandgap semiconductor with a bandgap exceeding 3 eV in single and few layer form. Its oxide, gallium oxide (Ga_2O_3), combines large bandgap (4.4-5.3 eV) with high dielectric constant (~10). Despite the technological potential of both materials, controlled oxidation of atomically-thin β-GaS remains under-explored. This study focuses into the controlled oxidation of β-GaS using oxygen plasma treatment, achieving ultrathin native oxide (GaS_xO_y, ~4 nm) and GaS_xO_y/GaS heterostructures where the GaS layer beneath remains intact. By integrating such structures between metal electrodes and applying electric stresses as voltage ramps or pulses, we investigate their use for resistive random-access memory (ReRAM). The ultrathin nature of the produced oxide enables low operation power with energy use as low as 0.22 nJ per operation while maintaining endurance and retention of 350 cycles and 10^4 s, respectively. These results show the significant potential of the oxidation-based GaS_xO_y/GaS heterostructure for electronic applications and, in particular, low-power memory devices.

Introduction

Gallium oxide (Ga_2O_3), a wide bandgap semiconductor, has emerged as a material of significant interest to the semiconductor industry owing to its excellent chemical and electrical properties. Its

wide bandgap of 4.4 to 5.3 eV[1-5], in addition to its thermal and chemical stability, made Ga_2O_3 applications in electronics very versatile. Notably, β-Ga_2O_3 boasts a high breakdown field strength of up to 8 MVcm^{-1} [6], a fact that fuelled the investigation into its applications in high-power electronics. Beyond conventional electronics, Ga_2O_3 has demonstrated tremendous potential in resistive switching (RS) applications due to its high intrinsic resistance and sensitivity to oxygen content[7-9]. The latter is more predominantly observed in amorphous Ga_2O_3, and low-power uni- and bipolar switching has been achieved in Ga_2O_3 memristors[10-16].

Nevertheless, the fabrication of ultra-thin, high-quality film of Ga_2O_3 remains a challenge. To this end, several techniques have been explored, such as the mechanical exfoliation of large Ga_2O_3 crystals and the squeezing of liquid Gallium metal[15-17]. However, the previously reported techniques, while promising, still face many challenges, such as the potential for scalability. A rarely explored scalable approach to obtain ultra-thin Ga_2O_3 is through the oxidation of a 2D layered material containing Ga metal[18]. Oxidation of 2D materials has been shown to produce ultra-thin oxide with high dielectric constant and clean interface in materials such as HfS_2[19,20], $HfSe_2$[21], TaS_2[22], $ZrSe_2$[21], and Bi_2O_2Se[23]. Oxidation techniques spanning thermal[21-23], oxygen plasma[19,20], and photo-oxidation[24] have been explored, with Plasma oxidation standing out for its ability to produce uniform dielectric layers. Furthermore, using a standard resist mask allows precise control of the location of oxidation, offering enhanced fabrication flexibility and tailored device functionality.

Group III monochalcogenides layered materials in X-M-M-X (M = Ga, In and X = S, Se, Te) form present a promising platform for electronic device applications[25-28]. More importantly, it has been reported that a good number of Ga-based group III monochalcogenides form a stable native Ga_2O_3[29,30]. One of the members of the monochalcogenides group that is generally neglected is hexagonal-layered gallium (II) sulfide (GaS), commonly referred to as β-GaS. A wide band-gap 2D material, GaS, has found its footing in applications such as optoelectronics[25,26,31]. In line with other layered monochalcogenides, GaS can be oxidised despite not being as rapid as GaSe or InSe[18]. However, reports on the oxidation mechanism of GaS are scarce and primarily focus on incidental environmental exposure rather than controlled oxidative processes[18].

This study investigates gallium oxide (GaS_xO_y) and GaS_xO_y/GaS structures produced by oxidising GaS via plasma oxidation under carefully controlled conditions and their use in resistive memories. Plasma oxidation of GaS resulted in ultra-thin amorphous GaS_xO_y while keeping the GaS layers beneath intact. Resistive-random-access memory (ReRAM) based on GaS_xO_y/GaS heterostructure exhibited low switching voltages and respectable endurance and retention.

Results and Discussion:

Figures 1 (a-c) show a schematic of the GaS oxidation process using RF oxygen plasma at room temperature. Multilayer GaS flakes are mechanically exfoliated (as described in the methods section) on a SiO₂/Si substrate. The flakes are then exposed to 10 W of O_2 plasma at 10 sccm and 20 mTorr, which alters the top layers of the flake chemically by converting them into a thin oxide layer. The chemical alteration can be deduced optically by observing a colour change in the flake post-oxidation in which the colour appears more translucent as the thickness of the oxide increases (Fig1 (d) and (e)). The final product could be partially or fully oxidised, depending on the oxidation conditions, time, and the initial GaS flake thickness. Figure 1 (f) shows the Raman spectra of three GaS flakes at different oxidation levels, which are pristine, partially oxidised, and fully oxidised in addition to the spectrum of the SiO₂/Si substrate for reference. While both pristine and partially oxidised GaS show the characteristic A^1_{1g}, A^2_{1g}, and E^1_{2g} peaks, fully oxidised flake shows no characteristic peaks of GaS, as shown in Fig 1 (f).
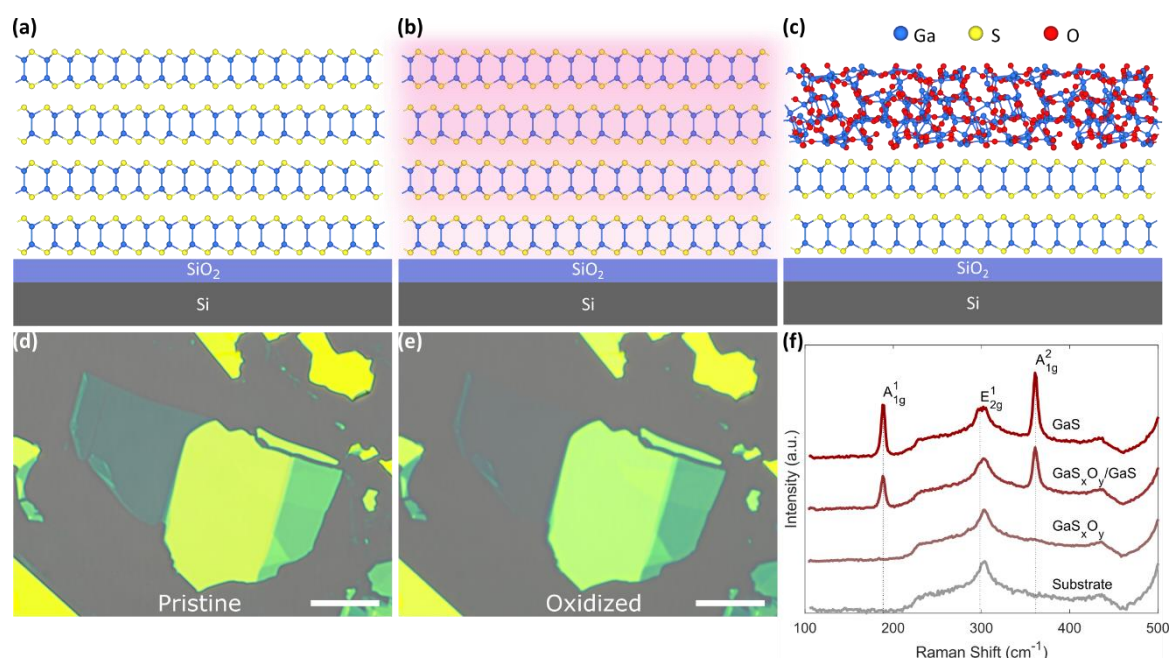

Figure 1: Schematic representation of the oxidation process in GaS. (a) Exfoliation of the GaS flake onto a SiO₂/Si substrate. (b) Oxygen plasma exposure of the exfoliated GaS flake. (c) Conversion of the topmost layers into GaSₓOᵧ. (d) and (e) shows optical microscope images of a pristine and an oxidised GaS flake on SiO₂/Si substrate with on 285 nm SiO₂. The sample was oxidised at 10 W of O_2 plasma at 10 sccm and 20 mTorr for 15 mins and show a clear colour change post-oxidation (scalebar 10 μm). (f) Raman spectra of three different GaS flakes at different oxidation levels. Pristine GaS and partially oxidised GaSₓOᵧ/GaS show the characteristic A^1_{1g}, A^2_{1g}, and E^1_{2g} peaks, whereas fully oxidised GaSₓOᵧ shows no characteristic peaks. The spectrum of SiO2/Si substrate in shown in grey.

To further characterise GaS and GaSₓOᵧ, spectroscopic imaging ellipsometry (SIE) was utilised as described in the methods section. To this end, A ~10.3 nm pristine GaS flake (kept in an oxygen-free environment during measurement) and a fully oxidised ~2.4 nm GaSₓOᵧ (both exfoliated on SiO₂/Si

substrate) were used for the measurements. The Tauc-Lorentz oscillator model was employed to fit the GaS data [32], whereas the Cauchy dispersion model was utilised for the GaS_xO_y.

Figure 2(a) shows the Tauc-Lorentz oscillator model fit of the ψ and Δ of the GaS. From the model, the bandgap was estimated to be 2.44 ± 0.15 eV, which is in good agreement with previous reports [31,33]. Due to the limited energy range used for this measurement, no interband transition peaks were observed in the dielectric response (Fig 2(b)). The Cauchy dispersion, shown in Fig. 2(c), fits well to the transparent GaS_xO_y. The refractive index (n), shown in Fig. 2(d), differs from the typical refractive index reported for amorphous Ga_2O_3. For example, at 600 nm wavelength, fully oxidised GaS_xO_y exhibit n ~1.6, whereas the n value reported in the literature for amorphous Ga_2O_3 sits in the range of 1.75-1.9[34-36]. This observation suggests that the oxidised GaS is of lower density, leading to a lower refractive index[37].
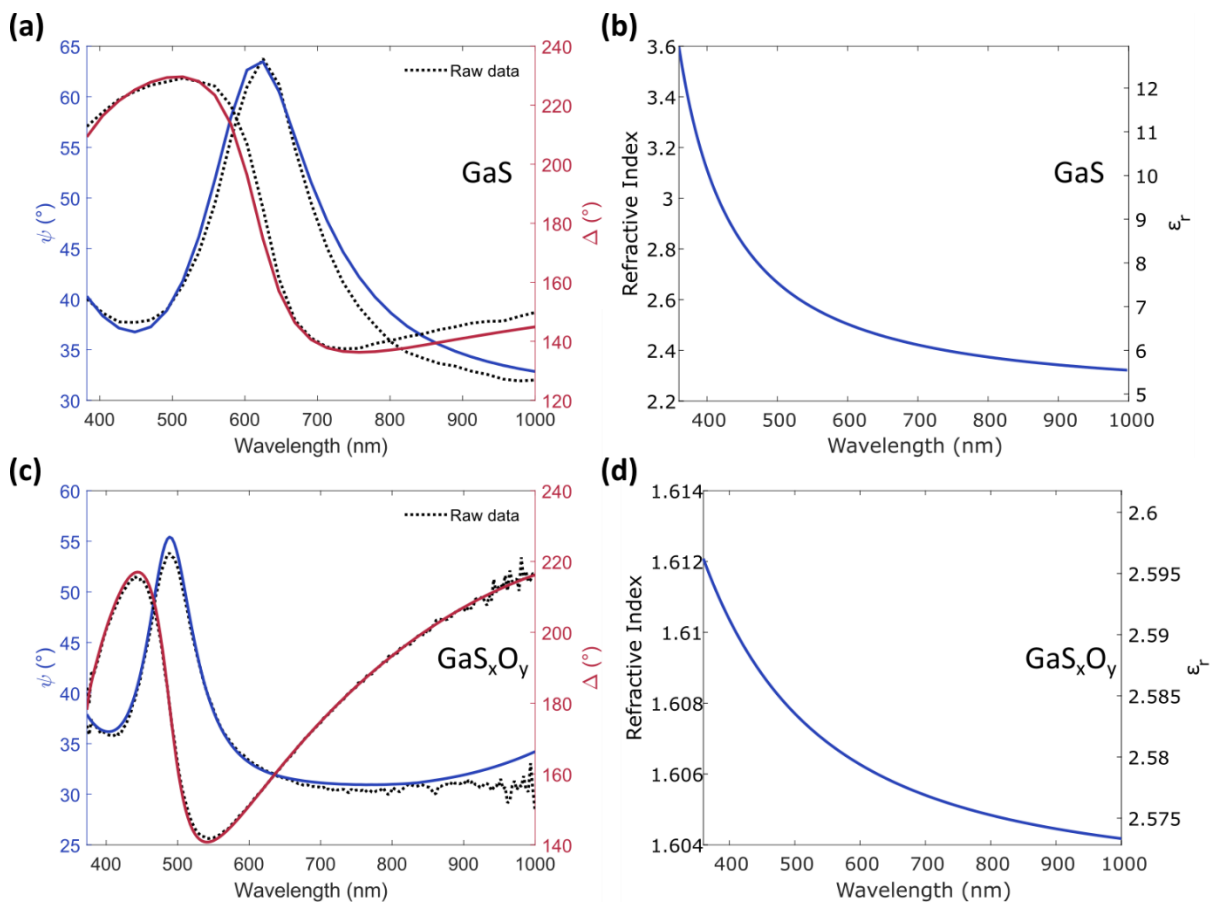
Figure 2: Spectroscopic imaging ellipsometry (SIE) of GaS and GaS_xO_y. (a) The ψ and Δ spectra fitted using the Tauc-Lorentz oscillator model (A = 94.3 ± 17.2 eV, E_0 = 4.133 ± 0.004 eV, E_g = 2.44 ± 0.15 eV, and Γ = 0.05 ± 1 eV). (b) is the corresponding refractive index and the real part of the dielectric response. (c) The ψ and Δ spectra of GaS_xO_y fitted using the Cauchy dispersion model (A = 1.603 ± 0.005, B = 1177 ± 1327 nm², C = 0 ± 1 nm⁴). (d) the refractive index and its corresponding real part of the dielectric response of the GaS_xO_y.

To further investigate the structure and chemical composition of the oxide, transmission electron microscopy (TEM) has been employed in conjunction with electron energy loss spectroscopy (EELS)

measurements. The TEM results provide an understanding of the material's atomic arrangements, while EELS maps provide the elemental distributions, allowing for a better understanding of the formed oxide nature. Figures 3 (a) and (b) show the cross-sectional TEM image of a partially oxidised GaS flake, subjected to 15-minute oxidation, distinctly showing the formation of oxide/semiconductor (GaS_xO_y/GaS) heterostructure with an oxide thickness of roughly 4 nm. The oxide derived in this manner is amorphous in nature, similar to oxides produced by oxygen plasma oxidation of other 2D materials[19,38]. Notably, the plasma oxidation does not damage the lattice of the unoxidised GaS which appears beneath the oxidised GaS. This is confirmed by in-plane TEM images of partially oxidised GaS flake, which were transferred on a Silicon Nitride (SiN_x) TEM grid before the oxidation. Here, the unoxidised GaS retains its inherent hexagonal crystalline structure, with the damage appearing minimal (Fig. 3(c)). This observation aligns well with the diffraction patterns presented in Fig. 3(d). In Fig. 3(e), we show the high-angle annular dark-field scanning TEM (HAADF-STEM) region from the same partial oxidised GaS flake as shown in Fig. 3(a,b). Figs. 3(f)-(h) presents the EELS elemental maps for Ga, S, and O corresponding to the imaged region in Fig. 3(e). These EELS results corroborate our earlier assertion that the partially oxidised GaS forms an oxide/semiconductor (GaS_xO_y/GaS) heterostructure, where the top layer undergoes oxidation while the bottom layer is minimally changed. However, the results also demonstrate that while there is a clear separation between the GaS and the GaS_xO_y layers, the GaS_xO_y still contains some sulfur species, as shown in Fig 3(g), and hence the designation GaS_xO_y.
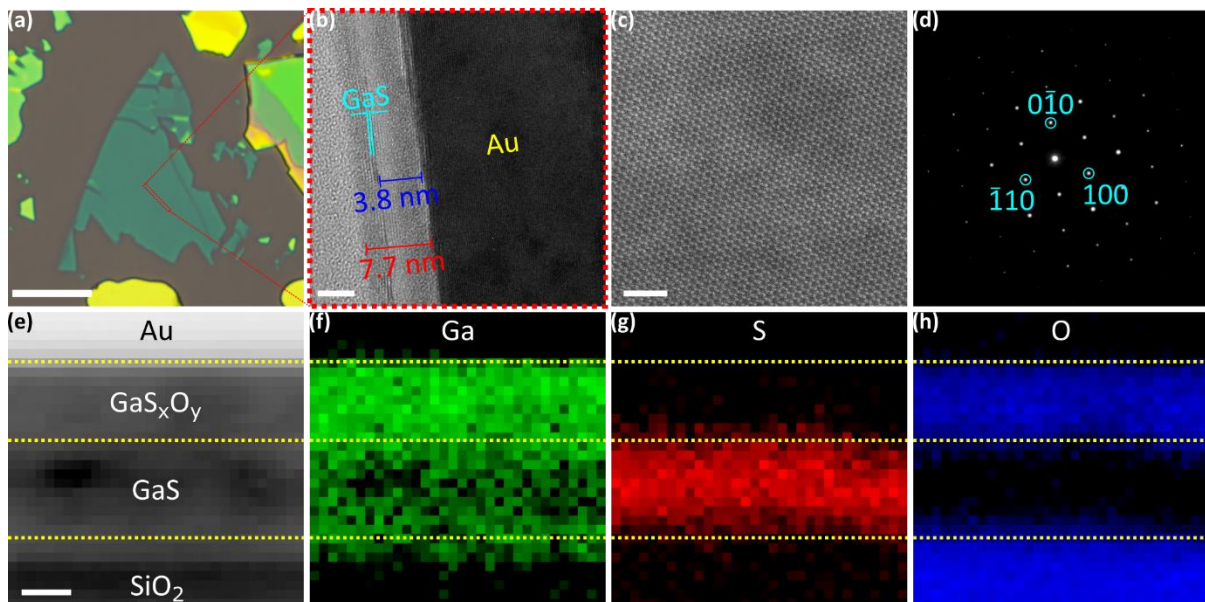
Figure 3: TEM images of partially oxidised GaS flake that was oxidised for 15 mins. (a) and (b) shows the optical image of the GaS_xO_y/GaS flake and its corresponding cross-section TEM image. The TEM image shows the formation of an amorphous layer on top of the crystalline GaS (scale 10 μm for optical and 3.8 nm for TEM). (c) and (d) HR-STEM image of a GaS_xO_y/GaS flake and its diffraction pattern confirming that the unoxidised GaS layers exhibit minimal damage (scale 2 nm). (e)-(h) HAADF-STEM image and its EELS elemental map of the flake from (a) showing the dominant sulfur and oxygen domain corresponding to the unoxidised GaS and the GaS_xO_y layers, respectively (scale 2 nm).

As shown in Figs. 4(a) and (b), the TEM images of the GaS$_x$O$_y$ produced at different oxidation times indicate that the oxide thickness after 10 and 15 minutes of oxidation is almost indistinguishable, which could indicate a self-limiting mechanism for oxidation at the given oxidation parameters. The average oxide thickness for both oxidation times was found to be ~3.8 nm, with a standard deviation of ~0.37 nm (Fig. 4(c)). In the context of device fabrication, the oxidation technique demonstrated here presents a significant advantage by reliably producing ultra-thin oxide layers while exhibiting a wide tolerance for variations in oxidation times.
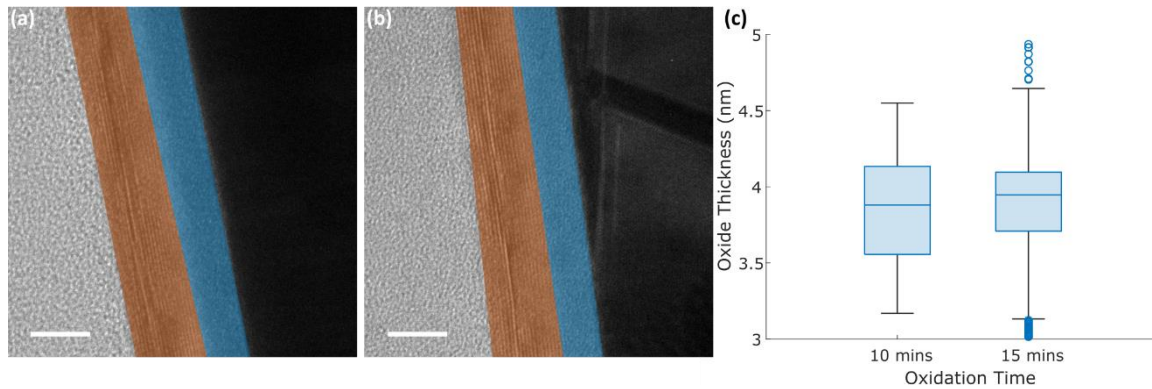

Figure 4: Time-dependent oxide thickness. (a) and (b) are false colour TEM cross-sectional images of 10 and 15 mins oxidation time, respectively. The GaS region was highlighted in orange, while the GaS$_x$O$_y$ region was highlighted in blue (scale 5 nm). (c) The calculated oxide thicknesses of 10 and 15 mins oxidation demonstrating near identical average and distribution (open circles are for thickness outliers, see Methods).

In the landscape of low-power electronics, the push for more efficient, compact, and faster memory technologies has been endless. Memristors stand out in this domain as promising candidates due to their unique ability to retain their resistance state based on applied voltage or current history[39]. At the forefront of this innovative frontier is the ReRAM, a distinct paradigm of switching memory technology. Beyond their evident advantages in terms of speed, endurance, and device density, ReRAM devices present a deceptively simple architecture[40-43]. This convergence of attributes makes ReRAMs key candidates for leading the advancement in low-power memory systems. Conventionally sputtered or deposited Ga$_2$O$_3$ has shown great potential in resistive switching applications with both uni- and bipolar behaviour observed[10-14,16]. In addition, recently, partially oxidised 2D materials such as HfS$_2$, HfSe$_2$, and PdSe$_2$ have shown promise for these applications[38,44-46], which motivated us to explore the use of the GaS$_x$O$_y$/GaS heterostructure in ReRAM applications.

As described in the methods section, the GaS$_x$O$_y$/GaS ReRAMs were fabricated using a 50 nm Au bottom electrode and a 90/10nm Au/Ti top electrode. Due to the small footprint of each device (~4 μm^2), multiple devices were made from the same flake. However, rather than using a standard crossbar array of multiple write lines (WL) and bit lines (BL), we used a single common BL to avoid sneak current paths from forming, as shown in Fig.5 (a). Figure 5 (b) shows typical DC I-V

characteristics of GaS_xO_y/GaS ReRAM oxidised for 10 mins where the voltage bias is applied to the bottom electrode. The device exhibits a bipolar switching behaviour, switching from a high resistive state (HRS) to a low resistive state (LRS) with a negative DC I-V sweep and from LRS to HRS using a positive DC sweep. The low SET (V_{SET}) and RESET voltages (V_{RESET}) of -0.4 V and 0.3 V, respectively, can be attributed to several factors such as the ultra-thin (~4 nm) and low-density nature of the oxide in addition to the presence of mobile oxygen and sulfur ions. We note that all the 6 tested GaS_xO_y/GaS ReRAMs with Au/Ti top electrode start in LRS and, therefore, do not require a forming step, which is normally required for resistive memories[47-49]. This can be advantageous for resistive device applications as it eliminates the need for a separate circuit responsible for the forming step and avoids current overshoots. While the reason behind the forming-free behaviour is still unclear, it can be speculated that this could be a result of the lower density of the oxide and the potential access of mobile ions within the switching layer. To further investigate the GaS_xO_y/GaS ReRAM device performance, retention measurements were conducted. The device exhibits good retention at 0.2 V READ voltage, where we can see a clear separation of the resistive states for 10^4 s (Fig.5 (c)). To characterise the device switching behaviour, pulsed voltage stress (PVS) measurements approach was chosen. The PVS measurements was performed by applying 500 ns, -0.5 V SET pulses and 2 µs, 0.5 V RESET pulses on a different device on the same flake. The resistance was read using 2 µs, 0.2 V pulses having a 100 ns rise and fall time and 2 µs separation time as shown in Fig. 5(d). As shown in Fig. 5(e), The GaS_xO_y/GaS ReRAM shows a slight variation in states over 350 cycles using PVS measurements with an average HRS/LRS ratio of ~3. In addition, the cumulative distribution function (CDF) plot, shown in Fig. 5(f), confirms the observation from the endurance measurement where a clear window exists between HRS and LRS with no overlap at any point. In order to assess the potential of our GaS_xO_y/GaS ReRAM for low-power applications, we calculated the energy consumed per SET/RESET operation by numerical integrating the power consumed within the pulse width used. The device consumes, on average, 0.22 nJ and 0.51 nJ to SET and RESET respectively. It is worth noting that the energy consumed by the RESET step excluding the plateau region is on average 0.31 nJ. While this exceeds the desired energy target for these applications, we believe that further optimisation of the oxide/semiconductor structure can yield lower energy consumption.
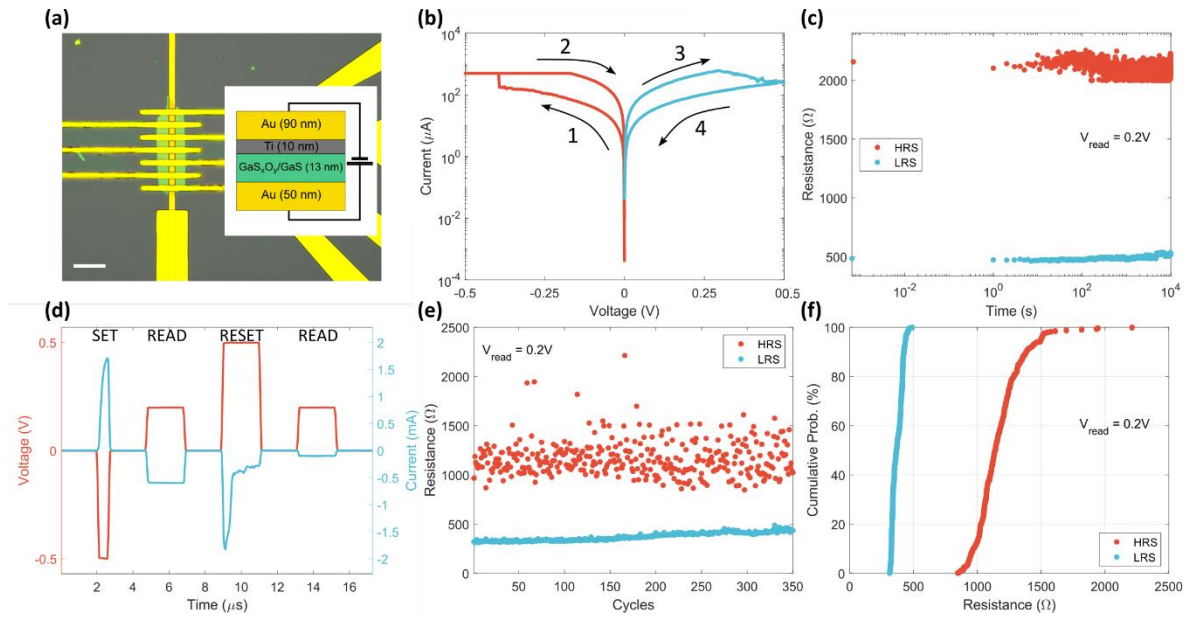
Figure 5: Oxidised GaS-based ReRAM element electrical characterisation. (a) Optical image of ReRAM element showing common bottom electrode with multiple top electrodes (scalebar: 10 μm). Inset is a schematic of the vertical stack ReRAM. (b) Typical DC switch cycle of ReRAM device where the device switches from HRS to LRS in the negative voltage regime and from LRS to HRS when voltage polarity changes. (c) resistance state retention over time measured at 0.2 V showing stable separation between HRS and LRS for 10^4 s. (d) a representative single PVS SET and RESET measurement cycle of voltage and current showing a SET step followed by READ, and RESET step followed by another READ. (e) and (f) shows endurance measurement and corresponding CDF plots read at 0.2V.

Understanding the performance of ReRAM devices requires not only an examination of their electrical characteristics, but also a deeper insight into their switching mechanisms. Different device architectures exhibit varied level of complexity, which critically influence device performance. The fact that GaS_xO_y/GaS ReRAM has an additional interface which is the oxide/semiconductor one suggests that the switching mechanism is far more complex. In the case of Ti-based Ga_2O_3 resistive switching devices, the commonly suggested mechanism for switching is via the conventional oxygen vacancy filament [9,12,50]. However, in GaS_xO_y/GaS ReRAM, such a simple explanation might not be applicable. First, the oxide layer in GaS_xO_y contains not only oxygen ions and their vacancies but also sulfur ions and their vacancies. While the oxygen ions have a smaller size compared to sulfur ions, which allows them to have higher mobility, determining the dominant conduction-driving ion depends on other factors, such as ions' concentration and the energy barrier for their movement within the oxide. However, a case can be made here for the oxygen ions based on the EELS results in Figs. 3(g) and (h). As the sulfur ions are more concentrated near the semiconductor while the oxygen ions are more abundant near the Ti top electrode, it is more likely to have the more mobile oxygen ions that are close to the Ti layer to contributing to the filament formation than the far and less mobile sulfur ions [38]. Nevertheless, it is also important to remember that the bottom semiconductor layer might have an active role in the switching. The role of the semiconductor layer is far more complex. While an oxide

7

layer is needed to have switching, it is observed in literature that the presence of the semiconductor layer improves the stability and endurance of the resistive switching behaviour in the device [38,45].

The complexity of the GaS_xO_y/GaS ReRAM extends to the explanation of the conduction mechanism. Previous reports on the Ti-based Ga_2O_3 memristors suggest a space charge limited conduction (SCLC) mechanism in the HRS and ohmic conduction in the LRS [12,16,50,51]. This assertion seems to hold true for the GaS_xO_y/GaS ReRAM (tested on another device with 10 nm GaS_xO_y/GaS), as shown in Fig. 6(a). The HRS show the characteristics of Space Charge Limited Current (SCLC) domains with an average slope for the ohmic region of ~1.1, indicating linear current-voltage (I-V) behaviour typical of ohmic conduction and a Child regime slope of ~1.95 over 97 DC-IV cycles, which reflects a quadratic I-V relationship typical of the trap-filled limited conduction. However, the LRS state also shows two domains with an expected ohmic region with a ~1.01 slope but an additional ~1.57 slope region. This suggests the LRS states have at least two conduction mechanisms potentially as a result of the semiconductor layer Fig. 6(b).

Ti-based top electrode plays a significant role in helping facilitate the formation of a stable conductive filament, which allows the GaS_xO_y/GaS ReRAM to exhibit a resistive switching behaviour [52]. To investigate the role of the Ti layer, another set of devices was made without a Ti layer, i.e. consisting of a stack of $Au/GaS_xO_y/GaS/Au$ as shown in Fig. 6(c). Devices based on this architecture failed to exhibit any stable bipolar switching behaviour. Initially, these devices may display one or two promising cycles with current compliance (I_{CC}) set at nanoampere levels but rapidly degrade to a state where no further switching behaviour can be observed. Hence, it can be concluded that the presence of Ti is crucial to facilitating the anionic filamentary formation [38]. Nevertheless, an unstable unipolar switching characteristic can be achieved under certain conditions, as shown in Fig. 6(c). It is unclear what drives such a switching mechanism in this type of device architecture. However, based on previous reports, an Au metallic filament could be responsible for the switching in memristors with only Au contacts [53,54].
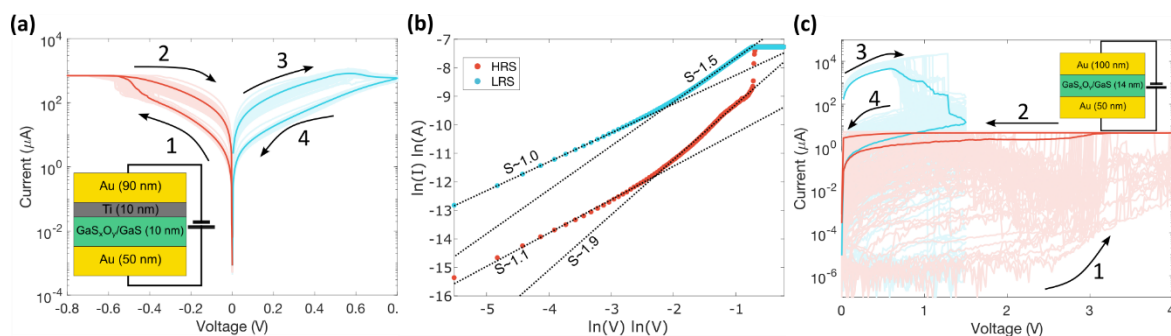
Figure 6: Electrode role in device switching in GaS_xO_y/GaS ReRAM. (a) DC IV sweep of the devices with light colours representing the cycles and the saturated colour curves representing the average. Inset is a schematic of the vertical stack ReRAM with 10 nm GaS_xO_y/GaS. (b) ln(I) vs ln(V) plot of a representative IV curve showing the characteristic SCLC domain

in HRS while also showing different domains in the LRS. (c) Unipolar DC switch cycle of Au only electrode GaS$_x$O$_y$/GaS ReRAM where light colours representing the cycles and the saturated colour curves representing the average. Inset is a schematic of the Au only vertical stack ReRAM.

Conclusions

In this study, we have successfully demonstrated the capacity to oxidise GaS, a representative of the group III monochalcogenides, via a controlled oxygen plasma treatment. Upon close inspection, it was discovered that the oxidation process starts at the surface and progressively moves inward. The resultant oxide is amorphous with a low density and contains some sulfur species doping. Intriguingly, this imperfect oxide composition has proven to be advantageous for ReRAM applications. Our evaluations of ReRAM devices that incorporated this oxide have shown significant potential combining forming-free operation with hours long retention, endurance of hundreds of cycles, and sub nano-Joule energy consumption. With further optimization of the oxidation and careful design of oxide-semiconductor we expect that such devices can play a significant role in low power electronics. Moreover, the oxidation method can be explored for applications beyond ReRAMs such as UV photodetectors and gas sensing.

Acknowledgements

Methods

GaS samples preparation:

GaS flakes were prepared by micromechanical exfoliation from bulk GaS crystal (HQgraphene). SiO_2/Si substrates were first cleaned using acetone, followed by isopropyl alcohol (IPA) and oxygen plasma treatment using an Advanced Vacuum–vision 320 RIE. The substrates were exposed to 100 W O_2 plasma at 40 sccm and 20 mTorr for 2 mins and then transferred into a glovebox with an Ar environment and O_2/H_2O level <0.1 ppm. The flakes were exfoliated immediately on the pre-treated substrate. Flakes of interest were identified using an optical microscope. Both exfoliation and optical microscope mapping of flakes were done in the same Ar environment.

GaS plasma oxidation:

Advanced Vacuum – vision 320 RIE was used to perform the O_2 plasma oxidation. Before placing the substrate, a 100 W O_2 plasma cleaning step was run at 40 sccm and 20 mTorr for 15 mins to clean the chamber. To reduce the effect of ambient oxidation, the samples were maintained inside the glovebox until the oxidation chamber was ready. The samples were exposed to ambient air for less than 30s. For oxidation, 10 W O_2 plasma was used at 10 sccm and 20 mTorr for 10 and 15 mins. Post oxidation, the samples were moved back immediately to the glovebox.

Device fabrication:

For device fabrication, a high resistivity (>10,000 Ω cm) Si substrate with 285 nm SiO_2 was used to prevent any unwanted current paths during pulse operations due to parasitic capacitances. Substrates were cleaned with acetone and IPA, followed by 100 W O_2 plasma at 40 sccm and 20 mTorr for 2 mins. Contacts were patterned by maskless photolithography utilising a Microtech LW405 laser writer. AZ-5214E image reversal photoresist was chosen for this purpose due to the ease of the lift-off process. Using Kurt J. Lesker PVD 200 Pro, a 50 nm Au bottom electrode was deposited. For lift-off, the substrates were left in an acetone bath overnight. GaS flakes were exfoliated on Si/SiO_2 substrate as described previously. Here, plasma treatment was skipped as it reduces the success rate of flake transfer. Selected flakes, identified by using an optical microscope, were transferred on top of the bottom electrode using a conventional dry transfer technique via Polydimethylsiloxane/polycarbonate (PDMS/PC) stamp[55]. Chloroform was used to remove any residual PC, followed by an IPA cleaning step. While the transfer was done in a glovebox, the chloroform step was done in ambient conditions. Extra care was taken to reduce sample exposure to oxygen during this process. Once transfer and cleaning were completed, the GaS flakes were oxidised as described above. The top electrode was fabricated following the same procedure described for the bottom electrode with the difference that electrode consisted of 10nm Ti and 90nm of Au. Ti was

deposited under ~1x10^{-7} mTorr pressure to prevent Ti oxidation. For the device shown in Fig, 5, only Au was used.

Electrical Measurements:

Keysight/Agilent B1500A semiconductor device parameter analyser was utilised for all electrical measurements. Voltage was always applied through the common bottom electrode, whereas the top electrode was grounded. A Keysight B1530A Waveform Generator/Fast Measurement Unit (WGFMU) module was used for pulse measurements in conjunction with a Remote-sense and Switch Unit (RSU). All measurements were done in ambient conditions at room temperature.

Raman Spectroscopy Measurements:

Raman measurements were performed using a Renishaw inVia microspectrometer. A 514.5 nm laser was used for all measurements with a 100X magnification lens and a 2,400 line/mm grating. The time and power during the Raman measurement were minimised to avoid unintentional photo-oxidation.

AFM Measurements:

The AFM measurements were conducted on a Bruker Dimension Icon AFM. Peak Force Tapping mode coupled with ScanAsyst algorithm was used for all the measurement.

Ellipsometry Measurements:

We conduct ellipsometry measurements using an EP4 Spectroscopic Imaging Ellipsometer from Park Systems Gmbh. The equipment is equipped with a laser-stabilized Xenon arc lamp and a three-grating monochromator as the spectroscopic light source. This allows for a spectral range between 360 nm to 1000 nm, with a 5 nm bandwidth of the output line. We use a polarisation state generator (PSG), consisting of a linear polariser and quarter-wave plate (compensator), to control the state of polarisation of the incident beam. The reflected light is collected through an analyser and a 50x objective to a 1392x1040 pixel CCD camera, which allows for a lateral resolution down to 1 μm. We perform all measurements in the P-A-nulling mode, where the compensator is kept fixed at 45°, and the polariser and analyser positions are shifted until the signal minimum is reached. Once the nulling condition is satisfied, we record the sample's ellipsometric angles Δ and ψ at each probing wavelength.

TEM Measurements:

To prepare samples for cross-sectional TEM measurement, we exfoliated GaS flakes on SiO$_2$/Si substrate as described above. The flakes were then oxidised to the desired time. To provide protection during the lamella preparation process, a double layer consisting of Au and aluminium oxide (AlO$_x$) was deposited using e-beam evaporation and ALD respectively. During the ALD step, extra care was taken to minimise temperature (which was kept below 150 ^{o}C) and time to prevent any modification

of the oxide. Lamellas were fabricated using a Dual Beam FIB-SEM system (Carl Zeiss Auriga) equipped with a platinum (Pt) deposition cartridge and nanomanipulator (Kleindiek Nanotechnik). The process started by depositing ~100 nm of platinum (Pt) as an additional protection deposited by e-beam evaporation (2 kV). This was subsequently overlaid with a micrometre-thick platinum layer deposited via a gallium ion beam. After the preliminary rough milling stage at 30 kV, the resulting plate, approximately 2 µm in thickness, was extracted and attached on the edge of a copper finger in a FIB lift-out grid. The lamella was subsequently thinned using a 15 kV ion beam to minimise ion beam-induced damage, resulting in a final lamella with a thickness under 100 nm. After thinning, the lamella was transferred to the TEM column for observation as soon as possible to minimise potential further oxidation.

The in-plane samples for (S)TEM were prepared by exfoliating GaS flakes as described above. The chosen flakes were then dry transferred using the PDMS/PC transfer method to silicon nitride (SiN_x) TEM grid with 1 µm diameter holes. Chloroform was used to remove PC residual. The transferred flake was then plasma oxidised as described above.

Transmission electron microscopy (TEM) and scanning TEM (STEM) was conducted on an uncorrected FEI Titan equipped with a Schottky field emission S-FEG source operating at 300 kV. Electron energy-loss spectroscopy (EELS) mapping was executed employing a Quantum Gatan Imaging Filter (GIF) detector, possessing an energy dispersion of 0.5 eV per channel.

To measure the oxide thickness from the TEM images, two flakes per oxidation time were used. To ensure that the TEM images are representative of the flake, at least 5 TEM cross-sectional images were taken per flake at different points. All 20 images were taken using the same magnification to ensure consistency. The images were then processed using purposely made MATLAB code to calculate the oxide thickness in each image. It should be noted that the code requires the user to define the boundaries of each region. To differentiate between the oxide and semiconductor layers, the user manually selects at least 10 points at the interface of the layers, and the code employs interpolation to create a detailed 100-point trace along the edge. The thickness measurement is subsequently based on the analysis of these 100 points, ensuring precise delineation between the amorphous oxide layer and the semiconductor.

1 Liao, Y., Zhang, Z., Gao, Z., Qian, Q. & Hua, M. Tunable Properties of Novel Ga(2)O(3) Monolayer for Electronic and Optoelectronic Applications. *ACS Appl Mater Interfaces* **12**, 30659-30669 (2020). https://doi.org/10.1021/acsami.0c04173

2 Su, J. *et al.* Unusual Electronic and Optical Properties of Two-Dimensional Ga2O3 Predicted by Density Functional Theory. *The Journal of Physical Chemistry C* **122**, 24592-24599 (2018). https://doi.org/10.1021/acs.jpcc.8b08650

3 He, H. *et al.* First-principles study of the structural, electronic, and optical properties ofGa2O3in its monoclinic and hexagonal phases. *Physical Review B* **74** (2006). https://doi.org/10.1103/PhysRevB.74.195123

4 Orita, M., Ohta, H., Hirano, M. & Hosono, H. Deep-ultraviolet transparent conductive β-Ga2O3 thin films. *Applied Physics Letters* **77**, 4166-4168 (2000). https://doi.org/10.1063/1.1330559

5 Tippins, H. H. Optical Absorption and Photoconductivity in the Band Edge ofβ−Ga2O3. *Physical Review* **140**, A316-A319 (1965). https://doi.org/10.1103/PhysRev.140.A316

6 Higashiwaki, M., Sasaki, K., Kuramata, A., Masui, T. & Yamakoshi, S. Gallium oxide (Ga2O3) metal-semiconductor field-effect transistors on single-crystal β-Ga2O3 (010) substrates. *Applied Physics Letters* **100** (2012). https://doi.org/10.1063/1.3674287

7 Bartic, M., Ogita, M., Isai, M., Baban, C.-L. & Suzuki, H. Oxygen sensing properties at high temperatures of β-Ga2O3 thin films deposited by the chemical solution deposition method. *Journal of Applied Physics* **102** (2007). https://doi.org/10.1063/1.2756085

8 Ogita, M., Higo, K., Nakanishi, Y. & Hatanaka, Y. Ga2O3 thin film for oxygen sensor at high temperature. *Applied Surface Science* **175-176**, 721-725 (2001). https://doi.org/10.1016/s0169-4332(01)00080-0

9 Guo, D. Y. *et al.* Evidence for the bias-driven migration of oxygen vacancies in amorphous non-stoichiometric gallium oxide. *AIP Advances* **7** (2017). https://doi.org/10.1063/1.4990566

10 Masaoka, N., Hayashi, Y., Tohei, T. & Sakai, A. Interface engineering of amorphous gallium oxide crossbar array memristors for neuromorphic computing. *Japanese Journal of Applied Physics* **62** (2023). https://doi.org/10.35848/1347-4065/acb060

11 Cui, D. *et al.* Coexistence of Bipolar and Unipolar Resistive Switching Behavior in Amorphous Ga₂O₃ Based Resistive Random Access Memory Device. *IEEE Electron Device Letters* **44**, 237-240 (2023). https://doi.org/10.1109/led.2022.3230247

12 Velpula, R. T., Jain, B. & Nguyen, H. P. T. Low-power multilevel resistive switching inbeta-Ga(2)O(3)based RRAM devices. *Nanotechnology* **34** (2022). https://doi.org/10.1088/1361-6528/aca418

13 Yang, Z. *et al.* Resistive random access memory based on gallium oxide thin films for self-powered pressure sensor systems. *Ceramics International* **46**, 21141-21148 (2020). https://doi.org/10.1016/j.ceramint.2020.05.191

14 Guo, D. Y. *et al.* Unipolar resistive switching behavior of amorphous gallium oxide thin films for nonvolatile memory applications. *Applied Physics Letters* **106** (2015). https://doi.org/10.1063/1.4907174

15 Wang, S. *et al.* Electronic synapses based on ultrathin quasi-two-dimensional gallium oxide memristor. *Chinese Physics B* **28** (2019). https://doi.org/10.1088/1674-1056/28/1/017304

16 Xu, Y. *et al.* Squeeze-Printing Ultrathin 2D Gallium Oxide out of Liquid Metal for Forming-Free Neuromorphic Memristors. *ACS Appl Mater Interfaces* **15**, 25831-25837 (2023). https://doi.org/10.1021/acsami.3c02998

17 Swinnich, E. *et al.* Flexible β-Ga2O3 Nanomembrane Schottky Barrier Diodes. *Advanced Electronic Materials* **5** (2019). https://doi.org/10.1002/aelm.201800714

18 Lu, Y. *et al.* Controlling Defects in Continuous 2D GaS Films for High-Performance Wavelength-Tunable UV-Discriminating Photodetectors. *Adv Mater* **32**, e1906958 (2020). https://doi.org/10.1002/adma.201906958

19   Jin, T. *et al.* Controlling Native Oxidation of HfS2 for 2D Materials Based Flash Memory and Artificial Synapse. *ACS Appl Mater Interfaces* **13**, 10639-10649 (2021). https://doi.org/10.1021/acsami.0c22561

20   Lai, S. *et al.* HfO2/HfS2 hybrid heterostructure fabricated via controllable chemical conversion of two-dimensional HfS2. *Nanoscale* **10**, 18758-18766 (2018). https://doi.org/10.1039/c8nr06020g

21   Mleczko, M. J. *et al.* HfSe2 and ZrSe2: Two-dimensional semiconductors with native high-kappa oxides. *Sci Adv* **3**, e1700481 (2017). https://doi.org/10.1126/sciadv.1700481

22   Chamlagain, B. *et al.* Thermally oxidized 2D TaS2 as a high-κ gate dielectric for MoS2 field-effect transistors. *2D Materials* **4** (2017). https://doi.org/10.1088/2053-1583/aa780e

23   Li, T. *et al.* A native oxide high-κ gate dielectric for two-dimensional electronics. *Nature Electronics* **3**, 473-478 (2020). https://doi.org/10.1038/s41928-020-0444-6

24   Peimyoo, N. *et al.* Laser-writable high-k dielectric for van der Waals nanoelectronics. *Sci Adv* **5**, eaau0906 (2019). https://doi.org/10.1126/sciadv.aau0906

25   Yang, S. *et al.* High performance few-layer GaS photodetector and its unique photo-response in different gas environments. *Nanoscale* **6**, 2582-2587 (2014). https://doi.org/10.1039/c3nr05965k

26   Late, D. J. *et al.* GaS and GaSe ultrathin layer transistors. *Adv Mater* **24**, 3549-3554 (2012). https://doi.org/10.1002/adma.201201361

27   Bandurin, D. A. *et al.* High electron mobility, quantum Hall effect and anomalous optical response in atomically thin InSe. *Nat Nanotechnol* **12**, 223-227 (2017). https://doi.org/10.1038/nnano.2016.242

28   Tamalampudi, S. R. *et al.* High performance and bendable few-layered InSe photodetectors with broad spectral response. *Nano Lett* **14**, 2800-2806 (2014). https://doi.org/10.1021/nl500817g

29   Beechem, T. E. *et al.* Oxidation of ultrathin GaSe. *Applied Physics Letters* **107** (2015). https://doi.org/10.1063/1.4934592

30   Schmidt, C., Rahaman, M. & Zahn, D. R. T. Conversion of 2-dimensional GaSe to 2-dimensionalbeta-Ga(2)O(3)by thermal oxidation. *Nanotechnology* **33** (2021). https://doi.org/10.1088/1361-6528/ac2f5d

31   Ho, C. H. & Lin, S. L. Optical properties of the interband transitions of layered gallium sulfide. *Journal of Applied Physics* **100** (2006). https://doi.org/10.1063/1.2358192

32   Jellison, G. E. & Modine, F. A. Parameterization of the optical functions of amorphous materials in the interband region. *Applied Physics Letters* **69**, 371-373 (1996). https://doi.org/10.1063/1.118064

33   Gutierrez, Y., Giangregorio, M. M., Dicorato, S., Palumbo, F. & Losurdo, M. Exploring the Thickness-Dependence of the Properties of Layered Gallium Sulfide. *Front Chem* **9**, 781467 (2021). https://doi.org/10.3389/fchem.2021.781467

34   Liu, W. *et al.* Thickness dependent optical properties of amorphous/polycrystalline Ga2O3 thin films grown by plasma-enhanced atomic layer deposition. *Thin Solid Films* **766** (2023). https://doi.org/10.1016/j.tsf.2022.139655

35   Gao, X. *et al.* Effect of top electrode materials on bipolar resistive switching behavior of gallium oxide films. *Applied Physics Letters* **97** (2010). https://doi.org/10.1063/1.3501967

36   Yang, H. *et al.* Effects of growth temperature and thickness on structure and optical properties of Ga2O3 films grown by pulsed laser deposition. *Superlattices and Microstructures* **131**, 21-29 (2019). https://doi.org/10.1016/j.spmi.2019.05.028

37   Ilhom, S. *et al.* Low-Temperature As-Grown Crystalline beta-Ga(2)O(3) Films via Plasma-Enhanced Atomic Layer Deposition. *ACS Appl Mater Interfaces* **13**, 8538-8551 (2021). https://doi.org/10.1021/acsami.0c21128

38   Liu, L. *et al.* Low-Power Memristive Logic Device Enabled by Controllable Oxidation of 2D HfSe(2) for In-Memory Computing. *Adv Sci (Weinh)* **8**, e2005038 (2021). https://doi.org/10.1002/advs.202005038

39   Chen, Y. ReRAM: History, Status, and Future. *IEEE Transactions on Electron Devices* **67**, 1420-1433 (2020). https://doi.org/10.1109/ted.2019.2961505

40   Ielmini, D. & Wong, H. S. P. In-memory computing with resistive switching devices. *Nature Electronics* **1**, 333-343 (2018). https://doi.org/10.1038/s41928-018-0092-2

41   Yang, J. J., Strukov, D. B. & Stewart, D. R. Memristive devices for computing. *Nat Nanotechnol* **8**, 13-24 (2013). https://doi.org/10.1038/nnano.2012.240

42   Waser, R. & Aono, M. Nanoionics-based resistive switching memories. *Nat Mater* **6**, 833-840 (2007). https://doi.org/10.1038/nmat2023

43   Ambrosi, E., Bricalli, A., Laudato, M. & Ielmini, D. Impact of oxide and electrode materials on the switching characteristics of oxide ReRAM devices. *Faraday Discuss* **213**, 87-98 (2019). https://doi.org/10.1039/c8fd00106e

44   Yin, L. *et al.* Two-Dimensional Unipolar Memristors with Logic and Memory Functions. *Nano Lett* **20**, 4144-4152 (2020). https://doi.org/10.1021/acs.nanolett.0c00002

45   Li, Y. *et al.* In-Memory Computing using Memristor Arrays with Ultrathin 2D PdSeO(x) /PdSe(2) Heterostructure. *Adv Mater* **34**, e2201488 (2022). https://doi.org/10.1002/adma.202201488

46   Xhameni, A., AlMutairi, A. & Lombardo, A. in *2023 IEEE Nanotechnology Materials and Devices Conference (NMDC)*   529-531 (2023).

47   Sheng, X. *et al.* Low-Conductance and Multilevel CMOS-Integrated Nanoscale Oxide Memristors. *Advanced Electronic Materials* **5** (2019). https://doi.org/10.1002/aelm.201800876

48   Diokh, T. *et al.* Study of resistive random access memory based on TiN/TaOx/TiN integrated into a 65nm advanced complementary metal oxide semiconductor technology. *Thin Solid Films* **533**, 24-28 (2013). https://doi.org/10.1016/j.tsf.2012.11.124

49   Yang Yin, C. *et al.* Balancing SET/RESET Pulse for $>\hbox{10}^{10}$ Endurance in $\hbox{HfO}_{2}\hbox{/Hf}$ 1T1R Bipolar RRAM. *IEEE Transactions on Electron Devices* **59**, 3243-3249 (2012). https://doi.org/10.1109/ted.2012.2218607

50   Zhang, L., Yu, H., Xiong, L., Zhu, W. & Wang, L. The modification of ultraviolet illumination to resistive switching behaviors in Ga2O3 memory device. *Journal of Materials Science: Materials in Electronics* **30**, 8629-8635 (2019). https://doi.org/10.1007/s10854-019-01185-4

51   Sato, K., Hayashi, Y., Masaoka, N., Tohei, T. & Sakai, A. High-temperature operation of gallium oxide memristors up to 600 K. *Sci Rep* **13**, 1261 (2023). https://doi.org/10.1038/s41598-023-28075-4

52   Cox, H. R. J. *et al.* A nanoscale analysis method to reveal oxygen exchange between environment, oxide, and electrodes in ReRAM devices. *APL Materials* **9** (2021). https://doi.org/10.1063/5.0070046

53   Shen, Y. *et al.* Variability and Yield in h-BN-Based Memristive Circuits: The Role of Each Type of Defect. *Adv Mater* **33**, e2103656 (2021). https://doi.org/10.1002/adma.202103656

54   Chen, S. *et al.* Wafer-scale integration of two-dimensional materials in high-density memristive crossbar arrays for artificial neural networks. *Nature Electronics* **3**, 638-645 (2020). https://doi.org/10.1038/s41928-020-00473-w

55   Purdie, D. G. *et al.* Cleaning interfaces in layered materials heterostructures. *Nat Commun* **9**, 5387 (2018). https://doi.org/10.1038/s41467-018-07558-3